CHAPTER 6

Observation of antiferromagnetic ordering from muon spin resonance study and Kondo effect in Dy doped Bi_2Se_3 topological insulator

Chapter 6

6.1 Introduction

Magnetic topological insulators (MTI) attract great attention of scientific community due to their unique application in spintronics. Magnetically doped Bi_2Se_3 and Bi_2Te_3 have been vigorously studied with anticipation of interesting fundamental phenomena such as the quantum anomalous Hall effect, three-dimensional Weyl fermions, neutral Majorana fermions and magnetic monopole [112]–[114]. Magnetic doping in topological insulators (TIs) is expected to break time reversal symmetry (TRS) and to demolish the Dirac like dispersion [29], [30]. It has been observed that doping of magnetic elements such as Mn, Cr and Fe generate energy gap at the Dirac point (DP) by inducing the ferromagnetism into the crystal [1], [30], [151], [166]. However, so far, very few reports are available on antiferromagnetic (AFM) ordered TIs [141], [143], [167], [168]. Furthermore, it has been reported that the origin of AFM ordering is the surface state (RKKY interaction) whereas the origin of ferromagnetic (FM) ordering is either surface (RKKY) or bulk state (van Vleck FM). Recently, the realization of an AFM topological insulator in $MnBi_2Te_4$ has been reported [169]–[173]. According to theoretical and experimental studies, the T_N of $MnBi_2Te_4$ is about 25 K [174] and the surface band gap at DP below T_N is ~80 meV [174]–[176]. However, few recent experiments suggest small gap (< 20 meV), [177], [178] which is explained in terms of a deviation of the surface magnetic ordering from the bulk. These inconsistent results might be due to the complex space-varying magnetic structure in $MnBi_2Te_4$.

Furthermore, it is already reported that rare earth (RE) doped TIs are AFM ordered[141], [143], [167], [168], [179]. Moreover, RE ions unlike divalent ions do not induce holes in the compound on substitution of Bi^{3+} [31], [180]. Therefore, to investigate the effect only from magnetic ordering on the topological surface states (TSS) of the TIs

using RE moments is highly promising. The important feature of the AFM TI, such as $MnBi_2Te_4$, is that it can retain a modified version of TRS. In an antiferromagnet, the flipping of spins associated with time reversal changes the pattern of alternating spins. In this direction if the RE ion can be doped in bulk (i.e., the magnetic ordering is induced in bulk) then it may retain both the TSS and AFM order. Kim *et al*. observed AFM ground state in Gd-doped Bi_2Se_3 TI with T_N below 6 K [143], while a bulk paramagnetic (PM) state has been reported by Song *et al.* in $Bi_{1.98}Gd_{0.02}Se_3$ [179].

On the other hand, topological Kondo insulator idea brings a tempting resolution of a long-standing puzzle in the Kondo insulator SmB_6 [181], which had been known to show a low temperature resistivity plateau [182], and which could be generally accepted as a consequence of TSS [183], [184]. The topological insulating behavior comes from the hybridization between localized *f*-electrons and conduction electrons in these systems. Hence, magnetic dopant in topological insulator with localized *f*-electrons may lead variety of phenomena such as Kondo effect and weak localization (WL) to weak anti-localization (WAL) crossover. Generally, RE ions have large moment and well-shielded 4*f* shell, expected to behave like isolated magnetic impurities in the system. Therefore, a doped system with RE ions should remain PM. Although, measurements of RE doped systems have shown unexpected and complex magnetic properties [124], [185].

In the present chapter, we observed that Dy-doping induces AFM ordering in $Bi_{1.9}Dy_{0.1}Se_3$ and the muon spin resonance (μ-SR) studies suggested that the signal measured with magnetization shows magnetic properties of < 2(1)% of the sample. We have also observed Kondo effect and diminish in WAL effect with Dy-doping in Bi_2Se_3 topological insulator.

6.2 Experimental Details

The present sample $Bi_{1.9}Dy_{0.1}Se_3$ was grown by modified Bridgeman method. High purity of Bi (99.999%), Se (99.999%) and Dy (99.999%) were mixed in stoichiometric ratio and vacuum sealed in a quartz tube at a pressure of ~10^{-6} torr. Afterwards, the sealed quartz tube was placed inside the furnace and then slowly heated up to 950 ^{o}C and retained for 24 h. Thereafter, the furnace was cooled from 950 ^{o}C to 550 ^{o}C at the rate of 5 ^{o}C/h and again retained at 550 ^{o}C for 72 hours. Finally, furnace was slowly (60 ^{o}C/h) cooled down to the room temperature. The crystal structure was examined by X-ray diffraction (XRD) measurements. Magnetotransport measurements were carried out by physical properties measurement system (PPMS). Magnetic measurements were performed by quantum design SQUID magnetic properties measurement system (MPMS). Band structure was studied by angle-resolved photoemission spectroscopy (ARPES) measurements at the Hiroshima Synchrotron Radiation Center (HiSOR), Hiroshima University, Japan with a focused ultraviolet laser beam (photon energy of 6.3 eV, beam spot size of ~10 μm, energy resolution is $\Delta E < 4$ meV)) equipped with VG Scienta R4000 electron analyzer [103]. Samples were cleaved either at room temperature for XRD or in-situ (at 30K) in ultrahigh vacuum (better than 5×10^{-11} torr) for ARPES. A mirror-like surface was obtained after cleaving in both the cases. We have performed bulk μ-SR measurements on single crystals of the topological insulator (TI) $Bi_{1.9}Dy_{0.1}Se_3$ on the General Purpose Spectrometer [186] (GPS) at the Swiss Muon Source at the Paul Scherrer Institute (PSI) in Villigen, CH. Single, spin polarized muons are successively implanted into the sample where they stop and decay into a positron and two neutrinos with a lifetime of ~2.2 μs. Due to the parity violation of this weak decay, the emission direction of the positrons encodes the average

time evolution of the muon spin polarization and thereby allows us to use the muon as a local magnetic probe [187], [188].

6.3 Results and Discussion

6.3.1 Experimental Analysis

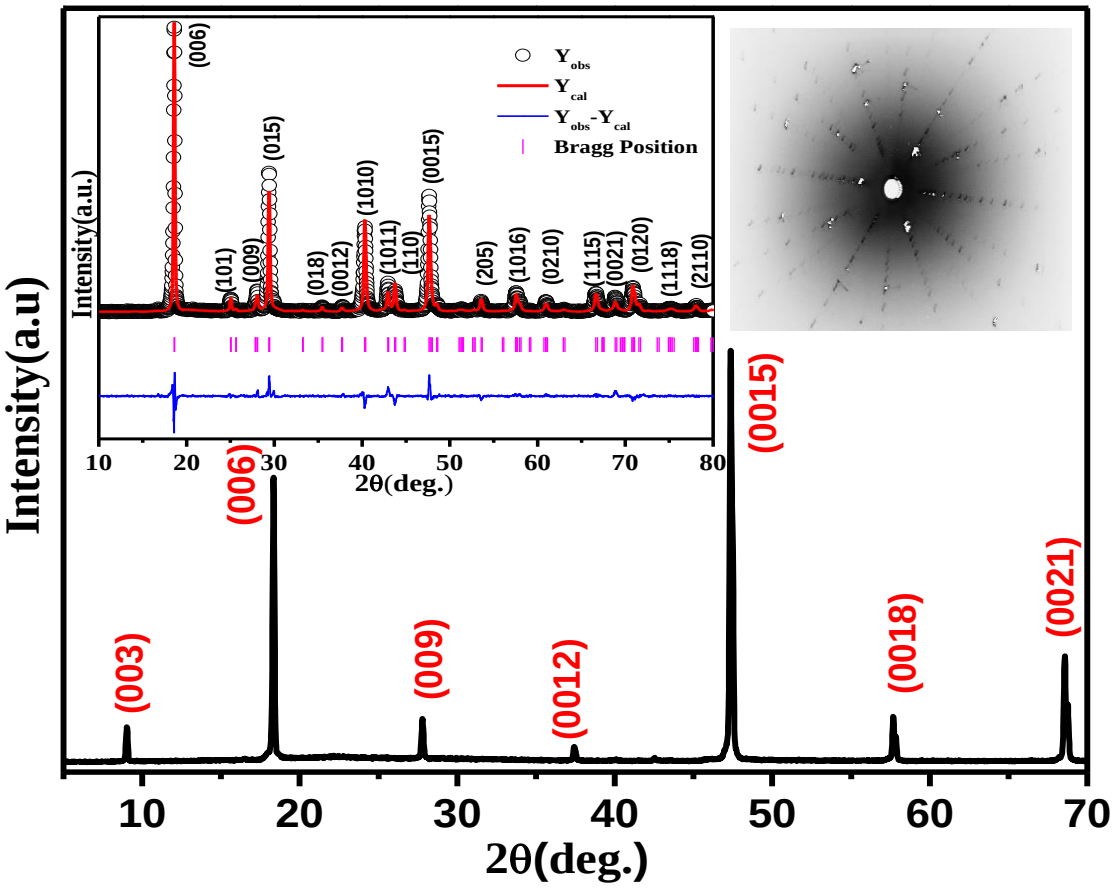

Figure 6.1: X-ray diffraction of $Bi_{1.9}Dy_{0.1}Se_3$ Single crystal sample cleaved along (*00l*) direction, Right Inset: Laue diffraction pattern, Left Inset: Rietveld refinement of powder XRD of $Bi_{1.9}Dy_{0.1}Se_3$ single crystal sample.

Figure 6.1 shows the X-ray diffraction (XRD) and Laue diffraction pattern (right inset) of a $Bi_{1.9}Dy_{0.1}Se_3$ single crystal. XRD reflects all diffraction peaks corresponding to the (*00l*) family of rhombohedral planes of Bi_2Se_3, indicating the sample is grown along '*c*' direction and the cleaved surface is an '*ab*' plane with no sign of secondary phases. We have performed Rietveld refinement of the powder XRD data of $Bi_{1.9}Dy_{0.1}Se_3$ single crystal

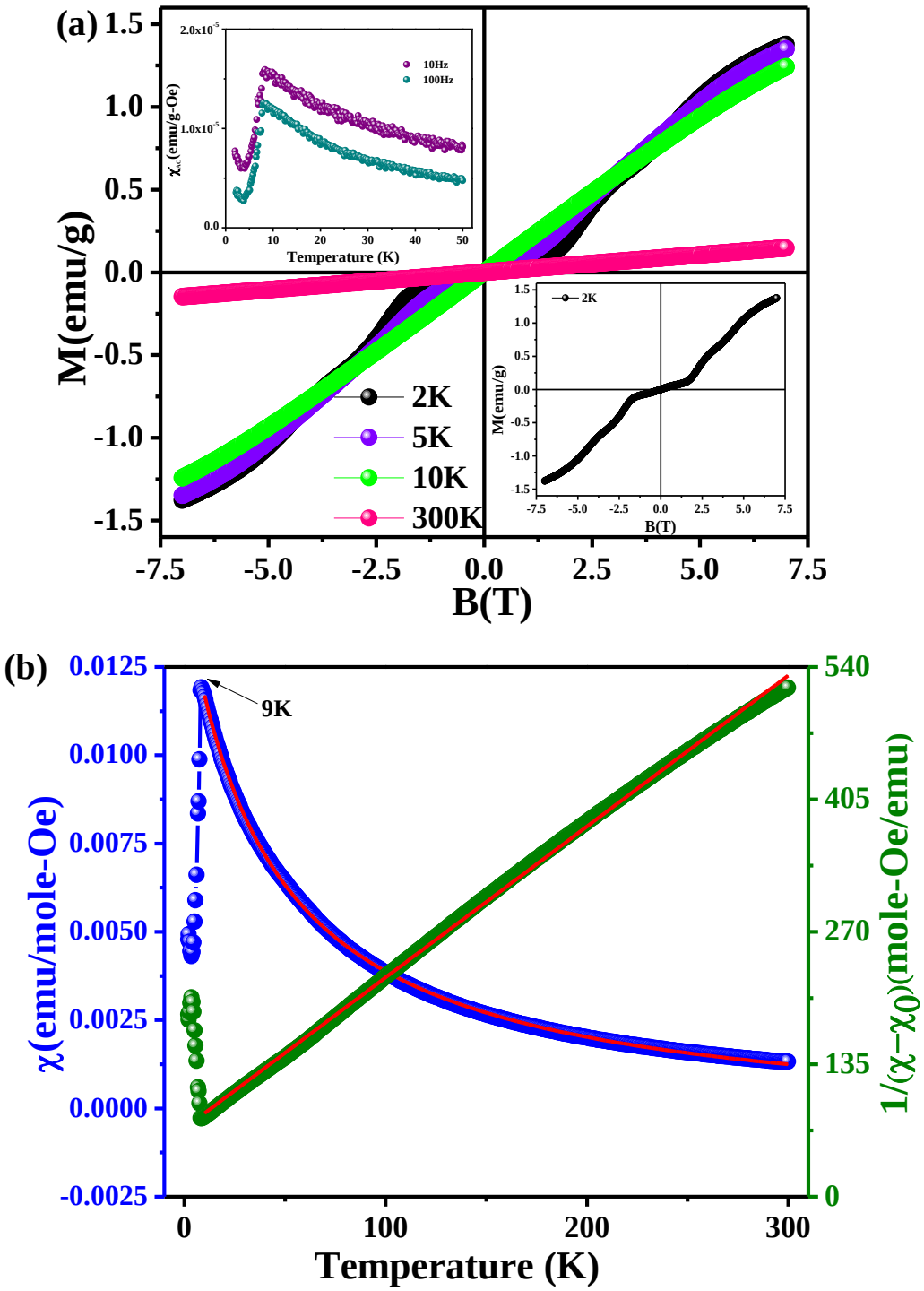

Figure 6.2: (a) Variation of magnetization (M) with magnetic field (B) for $Bi_{1.9}Dy_{0.1}Se_3$ at different temperatures, Top left Inset: AC magnetic susceptibility (χ'_{AC}) as a function of temperature at different frequencies (10 Hz and 100 Hz), Bottom right Inset: Field dependence of magnetization at 2 K. (b) Magnetic susceptibility (χ) as a function of temperature measured at 100 Oe applied magnetic field in zero field cooled (ZFC) condition and its inverse curve at right axis.

(left inset of figure 6.1) to obtain the lattice parameters. The determined lattice parameters are $a = b$ = 4.137(5) Å, c = 28.619(1) Å and cell volume is 424.299(3) Å^3 with the space group $\boldsymbol{D_{3d}^5}(R\bar{3}m)$, whereas the calculated α, β and γ values are 90˚, 90˚ and 120˚, which is close to pure Bi_2Se_3 [189].

In order to verify magnetic ordering in the sample, magnetic measurements were performed. The variation of magnetization (M) as a function of the magnetic field (B) at various temperatures is shown in the figure 6.2 (a). Magnetic susceptibility (χ) as a function of temperature was measured at 100 Oe applied magnetic field along c-axis in zero field cooled (ZFC) condition, which is shown in figure 6.2 (b). A clear transition can be seen around 9 K in $\chi(T)$, which may be attributed to PM to AFM transition. The susceptibility data can be fitted with Curie-Weiss law, $\chi(T) = \chi_0 + \frac{C}{(T-T_P)}$ where χ_0 represents temperature independent contribution of core diamagnetism and van-Vleck paramagnetism, C is Curie constant and T_P is the Curie-Weiss temperature. The linear dependence of $1/(\chi - \chi_0)$ with temperature is shown in figure 6.2 (b). A linear fit of Curie-Weiss law on $1/(\chi - \chi_0)$ in the temperature range 10 K - 300 K gives the value of C and T_P. The value of effective magnetic moment (μ_{eff}) per Dy ion can be evaluated from C, while T_P gives the information about the magnetic interaction. The calculated value of effective magnetic moment (μ_{eff}) per Dy ion with the help of fitting parameter C is 10.2 μ_B, which is close to the theoretical value 10.65 μ_B for Dy^{3+} ion. On the other hand, we have obtained the value of T_P = -45.3 K from the fitting. These results are indicating the presence of magnetic ordering as well as the substitution of Dy in Bi_2Se_3. The large negative value of T_P and sharp transition in $\chi(T)$ strongly suggests the long-range AFM ordering [143]. A clear non-linearity appears in magnetization vs. magnetic field curve at 5 K (shown bottom right inset

of figure 6.2 (a) at 2 K), which reflects a transition from AFM to FM at very low temperature (~5 K) at ~3 T magnetic field. Furthermore, the transition around 9 K is also reflected in χ_{AC} measurement at the frequency 10 Hz and 100 Hz (top left inset of figure 6.2 (a)). Similar results were obtained by others for doped TIs with magnetic impurities [141], [143], [167], [168].

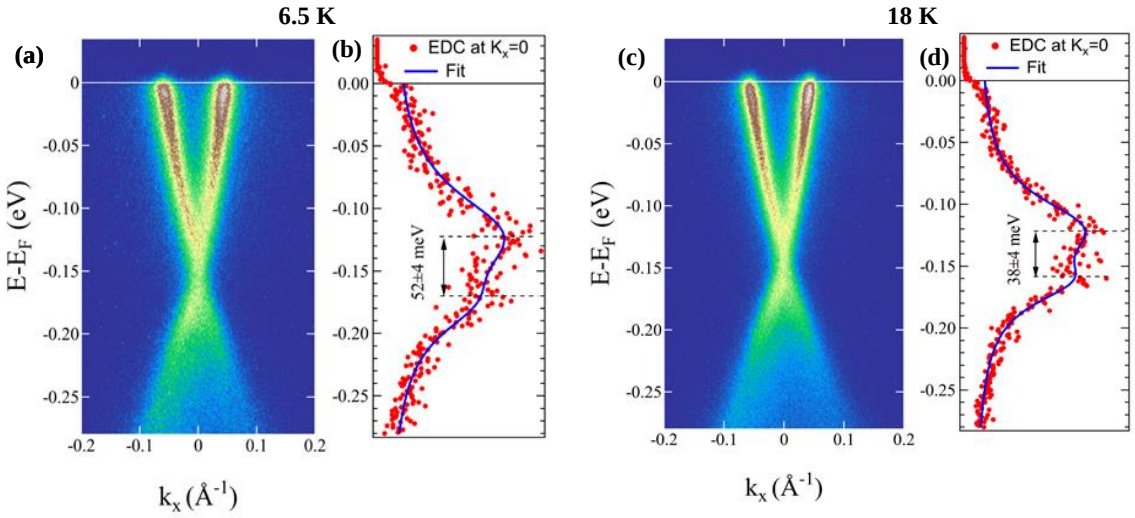

Figure 6.3: (a) Electronic band structure and (b) the EDC curve fit at 6.5 K, (c) Electronic band structure and (d) the EDC curve fit at 18 K for $Bi_{1.9}Dy_{0.1}Se_3$ single crystal sample.

To investigate the electronic structure and the doping effect on TSS, we have performed the ARPES measurement by Laser system. The ARPES measurement was carried out at 6.5 K (below magnetic ordering) as well as at 18 K (above PM to AFM transition). The X-shaped Dirac like TSS can be seen clearly in figure 6.3 (a, c). The position of the DP is found around ~144 meV below the Fermi level (E_F) and E_F lies very close to the bulk conduction band (BCB), suggesting *n*-type nature of the sample [4]. If the TRS is maintained, then TSS of Bi_2Se_3 connect the upper and lower part of Dirac cone at DP. The protection of TRS can be broken by magnetic doping which may generate the gap at the DP and may separate the upper and lower Dirac cones [30]. Unlike pure Bi_2Se_3 [30], we observed a gap opening at the DP in Dy-doped Bi_2Se_3 sample as illustrated in figure 6.3.

Hence, the dispersion of TSS is broken at DP, consequently double peak structure is observed in the energy distribution curve (EDC) at the $\bar{\Gamma}$ point (k_x=0). We have used the two Lorentzian functions for the fitting of the EDC at $k_x = 0$ as shown in figure 6.3 (b, d).

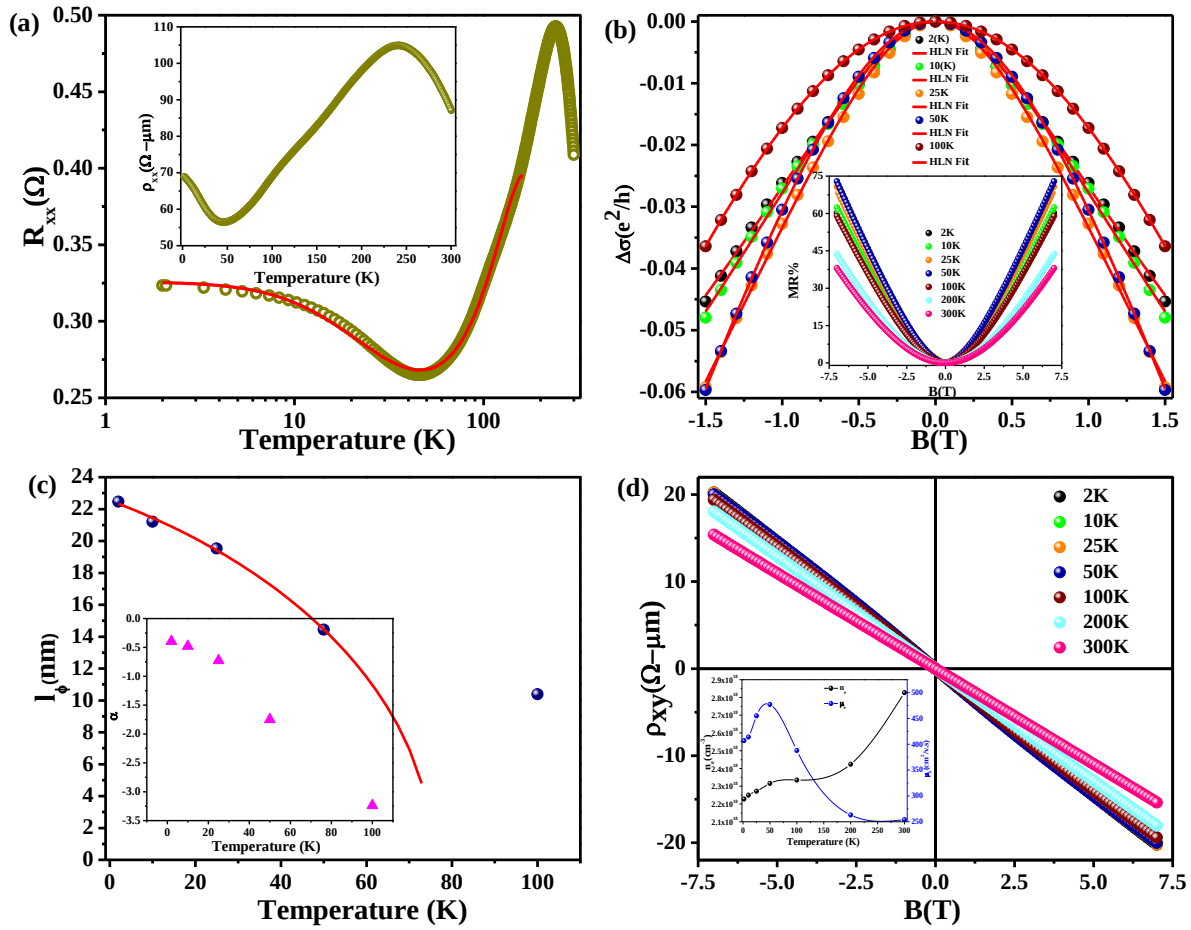

Figure 6.4: (a) Resistance vs temperature variation of $Bi_{1.9}Dy_{0.1}Se_3$, fitted with Kondo model, Inset: Variation of resistivity with respect to temperature, (b) Magnetoconductivity fitted with HLN equation at the low magnetic field (-1.5 T to 1.5 T), and at different temperatures, Inset: MR ratio (%) variation as a function of magnetic field for $Bi_{1.9}Dy_{0.1}Se_3$ at various temperatures. (c) Represents the change in phase coherence length with temperature, fitted with equation (4), Inset: Shows change in the value of prefactor (α) with temperature. (d) Field dependence of the Hall resistivity for $Bi_{1.9}Dy_{0.1}Se_3$. Inset: The variation of carrier concentration and carrier mobility as a function of temperature.

We have evaluated the upper limit of the gap to be ~52±4 meV at 6.5 K and ~38±4 meV at 18 K. The wide gap opening at lower temperature might be due to the induced magnetic

ordering. The observed gap opening is comparable to that of $MnBi_2Te_4$ below magnetic ordering [174], [176]–[178], [190].

The resistivity (ρ_{xx}) vs temperature (T) curve for $Bi_{1.9}Dy_{0.1}Se_3$ in temperature range 2 K to 300 K is shown in inset of figure 6.4 (a). An increase in resistivity with decreasing temperature can be seen in the low temperature region. This logarithmic increase in the resistivity with decreasing temperature is a characteristic feature of Kondo effect arising from the Dy magnetic impurity in the crystal. By plotting the resistance (R_{xx}) *vs*. temperature (T) independently one can clearly inspect logarithmic increase in the resistance with decreasing temperature below 50 K, as shown in figure 6.4 (a). The R_{xx}-T data of $Bi_{1.9}Dy_{0.1}Se_3$ was fitted using a simplified Kondo model given by

$$R_{xx}(T) = R_o + qT^2 + pT^5 + R_k\left(\frac{T}{T_k}\right) \tag{6.1}$$

Where, R_o is the residual resistance due to disorder in the sample, and the T^2 and T^5 terms are the electron-electron and the electron-phonon interactions respectively. For the numerical fitting of this model, we used an empirical form

$$R_k\left(\frac{T}{T_k}\right) = R_k(T=0)\left[\frac{T_k'^2}{T^2+T_k'^2}\right]^S \tag{6.2}$$

Where $T_k' = T_k/\left(2^{1/S}-1\right)^{1/2}$, parameter *s* depends on the spin of the impurity and it was fixed to 0.225 [191]–[194]. The obtained values from numerical fit [figure 6.4 (a)] of $R_{xx}(T)$ using Eqns. (1) and (2) are $R_o = 0.11067\ \Omega$, q = $1.25501\times10^{-5}\ \Omega/K^2$, p = $-1.07679\times10^{-12}\ \Omega/K^2$, $R_k(0) = 0.21531\ \Omega$ and $T_k = 73.9$ K. Figure 6.4 (a) clearly illustrates that the experimental data is well fitted by equation (1) with Kondo temperature ~74 K. However, this manifested, upturn in the resistivity at the low temperature may be due to the opening of a gap at the DP [141], [195]. However, the DP is well below the Fermi level, and the TSS does not have a gap at the Fermi level. Furthermore, the

magnitudes of the gap at the DP are 52 meV (~600 K) at 6.5 K and 38 meV (~440 K) at 18 K. The energy scale of the gap at the DP seems to be too large to relate it with temperature dependence of the resistivity below ~50 K. This suggests that the observed upturn is due to the Kondo effect. From the inset of figure 6.4 (a) one can notice a broad hump at temperature around 240 K. This high temperature resistivity hump either may be associated to plasmon-polaron formation and resistivity might be increased due to coulomb drag by the plasmon contribution [196]–[199] or may emerge from the reduction of antisite defects and enhancement in topological transport properties[90], [141], [200], [201].

Furthermore, in order to probe the TI property, magnetoresistance (MR) measurement has been performed. The MR ratio can be defined as $\left\{\frac{\rho_{xx}(B)-\rho_{xx}(0)}{\rho_{xx}(0)}\right\}$, where ρ_{xx}(B) and ρ_{xx}(0) are the resistivity values under non-zero and zero applied magnetic field (B) respectively. MR ratio (%) with respect to magnetic field (up to $\pm$ 7 T) at different temperatures is displayed in inset of figure 6.4 (b). Almost linear dependency on magnetic field (B) of MR data can be seen up to 50 K. At higher temperature, the dependency of MR data on magnetic field turns to parabolic. This confirms the quadratic dependency of MR on B above 50 K as shown in figure 6.4 (b). The linear dependency of MR on magnetic field below 50 K is suggesting the presence of weak anti-localization (WAL) effect below 50 K. When temperature increased above 50 K the dependence of MR on B switched from linear to quadratic nature, suggesting suppress in WAL effect and enhancement in Weak localization (WL) effect. Hence, apart from WAL effect which comes from the π-Berry phase of TSS, the signature of WL effect is also appeared at high temperature. Therefore, to understand the crossover from WAL to WL effect and the role of TSS, we have performed HLN [23] fit on magnetoconductivity (MC) data.

$$\Delta\sigma = \sigma(B) - \sigma(0) = A\left[\psi\left(\frac{1}{2} + \frac{h}{8\pi eBl_{\varphi}^{2}}\right) - ln\left(\frac{h}{8\pi eBl_{\varphi}^{2}}\right)\right] \quad (6.3)$$

Where, $A = \frac{\alpha e^2}{\pi h}$ represents the number of conduction channels present in the sample with $\alpha = -\frac{1}{2}$ per conduction channel and ψ is digamma function, l_φ is the phase coherence length. MC curves fitted with HLN formula in magnetic field range between -1.5 T to 1.5 T at different temperatures are shown in figure 6.4 (b). The obtained values of α and l_φ at different temperatures from HLN fitting are also shown in figure 6.4 (c). We have also examined the effect of electron-electron (*e-e*), electron-phonon (*e-p*) scattering on phase coherence length (l_φ) as a function of temperature. According to the WAL effect in 3D TIs, both the '*e-e*' and '*e-p*' scattering are supposed to be emerged [133], [134].

The temperature-dependent l_φ can be described as

$$\frac{1}{l_{\varphi}^{2}(T)} = \frac{1}{l_{\varphi}^{2}(0)} + A_{ee}T^{q_1} + A_{ep}T^{q_1'} \quad (6.4)$$

Where, $l_\varphi(0)$ is the phase coherence length at zero temperature, $A_{ee}T^{q_1}$ and $A_{ep}T^{q_1'}$ are the contribution from the *e-e* and *e-p* interactions, respectively. The values of l_φ, obtained from equation (3) at different temperatures are fitted with equation (4) by fixing $q_1 = 1$ for electron-electron scattering and $q_1' = 2$ for 2D electron-phonon scattering [128], [135] as shown in figure 6.4 (c). As we can see from figure 6.4 (c) that the fitting is deviating above 50 K, which may be associated to the reduction in WAL and enhancement in WL. The value of prefactor α is ranging from -0.4 (2 K) to -3.24 (100 K). For a typical WAL effect the value of α should be -0.5, the deviation in the value of prefactor suggest the contribution of bulk channel with increasing temperature [202], [203].

To perceive the nature of the transport carrier, we have performed Hall resistivity (ρ_{xy}) measurement as function of magnetic field (B) at different temperatures. Figure 6.4 (d)

shows linear behavior of ρ_{xy} with negative slope, suggesting that the transport carriers are electrons. This n-type nature may be observed due to anti-site defects and Se vacancies in the sample [90]. Evaluated value of carrier concentration (n_e) and carrier mobility (μ_e) from Hall data at different temperatures is also shown in inset of figure 6.4 (d). The value of n_e is varying from 2.2×10^{18} cm^{-3} (2 K) to 2.8×10^{18} cm^{-3} (300 K) and the value of μ_e lies in between 407 $cm^2/V.s$ (2 K) to 254 $cm^2/V.s$ (300 K) [62], [204].

In order to probe the local magnetic fields inside the sample in this magnetic phase, we have performed a zero-field μ-SR measurement at 1.6 K. The result is shown in figure 6.5 (a, b). Note that a dipolar field at the muon site would cause a Larmor precession of the muon polarization, causing oscillations to be present in the spectra. However, within the statistical error of the measurement, we see no such oscillation, figure 6.5 (a). The zero field spectra could be fitted with Musrfit [205] to an exponential damped polarization:

$$A(t) = A_0 e^{-\lambda t} \tag{6.5}$$

The initial asymmetry (A_0) was close to its maximal value and depolarization rate λ was 0.068(1) μs^{-1}. This value can be compared to very similar measurements on the quantum anomalous Hall system $V_{0.19}(Bi,Sb)_{1.81}Te_3$, which also did not exhibit coherent oscillations [206]. There, λ is 0.052(3) μs^{-1} at room temperature, but there is a much higher static depolarization (up to ~10 μs^{-1}) in the magnetic state [206]. Therefore, the zero field response of the 5% Dy doped Bi_2Se_3 crystal strongly resembles that of an undoped TI or a doped TI above its magnetic transition.

In order to get a more precise estimate of the ordered fraction of the sample, we performed measurements in a weak transverse field (wTF) of 5 mT perpendicular to the initial muon spin direction. The spectra can be described with a Gaussian damped oscillation at a frequency corresponding to the external field, see figure 6.5 (c).

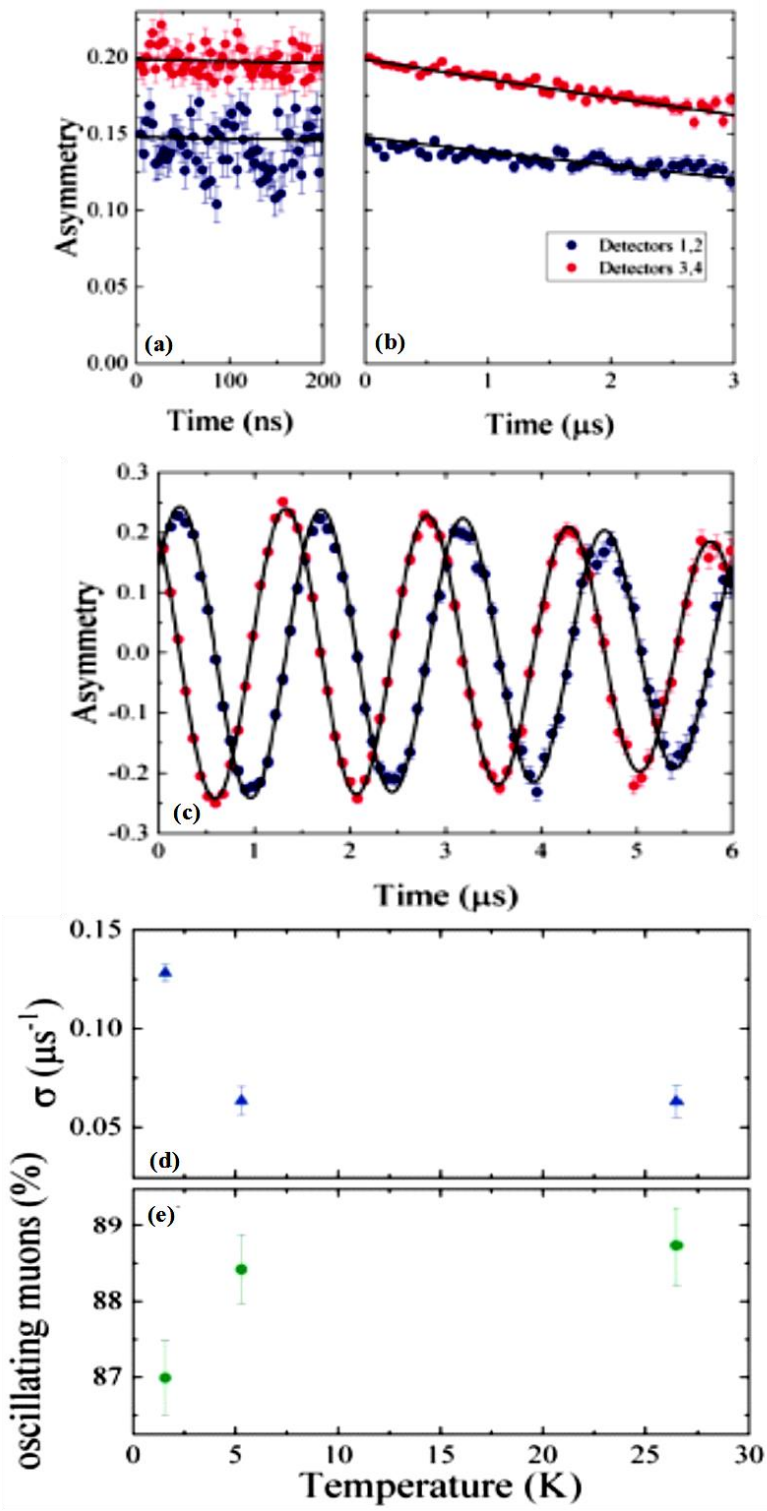

Figure 6.5: (a,b) μ-SR time spectra in zero field at 1.6 K. (a) shows a zoom into the first 200 ns of (b). (c) μ-SR time spectra at 1.6 K in a weak transverse field of 5 mT. The different colors represent different sets of opposite detectors. The solid black lines show fits to the data. (d) Depolarization rate in wTF as a function of temperature. (e) Oscillating fraction as a function of temperature, compared to a calibration measurement on Ag.

Therefore, the spectra were fitted with

$$A(t) = A_0 e^{-(\sigma t)^2/2} \cos(\gamma_\mu B t + \varphi) \quad (6.6)$$

where A_0 denotes the initial asymmetry, σ the depolarization rate, $\gamma_\mu = 2\pi \times 135.5$ MHz/T the muon gyromagnetic ratio, B the local field at the muon site and φ is a phase factor describing the measurement geometry. If the muon stops in a magnetic environment, it does not oscillate at the applied field, which leads to an effective loss in A_0. This has for example been observed in other Cr, V and Dy doped TI films [185], [206]. In figure 6.5 (e) we show the oscillating fraction, given by A_0 normalized by the maximal A_0 measured on an Ag-sample. Note that even at high temperature, A_0 is only about 89% of the maximal value. However, such a shift might also be affected by the sample size and position. Interestingly, at the magnetic transition observed in magnetization, the value of A_0 changes only marginally. At the same time, the depolarization rate σ [figure 6.5 (d)] increases, these points to a slightly broader distribution of internal fields, or enhanced dynamics. These measurements allow us to make estimate an upper limit of the muons stopping in a magnetic environment. Based on the decrease of A_0 between 5 K and 2 K, we estimate that at most 2(1)% of the sample orders magnetically. In addition, there are some stray fields from those magnetic regions, which cause the slight enhancement of σ.

6.3.2 Theoretical Analysis

In order to validate our measurement of AFM ground state, we additionally performed first-principle calculation based on density functional theory (DFT). We adopt Vienna ab-initio simulation package (VASP) [207] as a calculator which is based on pseudo-potential method. The pseudo-potentials of elements were computed by incorporating projected augmented wave (PAW) scheme into VASP. The Perdew-Burke-Ernzerh of (PBE) functional [161] of generalized gradient approximation (GGA) was chosen as electron

exchange-correlation functional in extracting ground state stability and electronic structure. Further, to expand plane wave basis sets, kinetic energy cutoff equal to 350 eV was employed. We set Γ - centered mesh of k-points of size 2×2×1 for atomic relaxation while self-consistent field calculations were carried out at 8×8×1 mesh of k-points. The gaussian smearing method along with smearing width of 0.10 eV was chosen for Brillouin zone integration. We follow energy convergence limit upto 1×10^{-5} eV for all set of calculations. Before to perform final calculations, the atomic positions of atoms are relaxed into cell at experimental lattice constants until the residual force on atoms reduces up to ≤ 0.01 eV $Å^{-1}$. The hexagonal cell of Bi_2Se_3 exhibits three quintuple-layers (QLs) and in each QL Se-Bi-Se-Bi-Se stacking sequence followed which is bonded by weak van der Waals (vdW) forces. Therefore, to incorporate weak vdW inter layer interaction between layers, we have included Grimme's density functional [208] into calculations which provide good description of bond length between atoms.

We adopt supercell approach for performing doping of Dy atoms at Bi sites. The supercell of size 2×2×1 was generated first and thereafter the energy minimization each configuration of two Dy atoms doped Bi_2Se_3 was performed by relaxing atomic positions. We have considered total six possible configurations in which Dy atoms resides at different atomic distances, lying into same or different layers and QLs. Interestingly, the ground state energy for each configuration is found to be lower for AFM state in comparison to FM states. This supports our experimentally observed AFM ordering. However, our calculated magnetic moment yields $\sim 4.75\ \mu_B$ per Dy atom. The total energy changes between least and most stable configurations among all considered configurations for AFM (FM) state comes equal to 64 (60) meV. Furthermore, the magnetic ordering for each configuration was estimated by employing expression: $\Delta E = \frac{1}{2}\left[E_{AFM} - E_{FM}\right]$; where E_{AFM} and E_{FM}

governs the ground state total energy of AFM and FM states, respectively. The calculated values of coupling states, including distance between two Dy atoms, have been summarized in Table 6.1. From Table, it is clear that the variation in magnetic ordering energy comes smallest for the third configuration which follows doping of two Dy atoms at first nearest neighbor sites at a distance of 4.26 Å lying into same QL and different Bi atomic layers. The calculated value of ΔE for this configuration comes -1.4 meV and thus represents strong magnetic ordering. Figure 6.6 (a) illustrates the configuration which is energetically most stable.

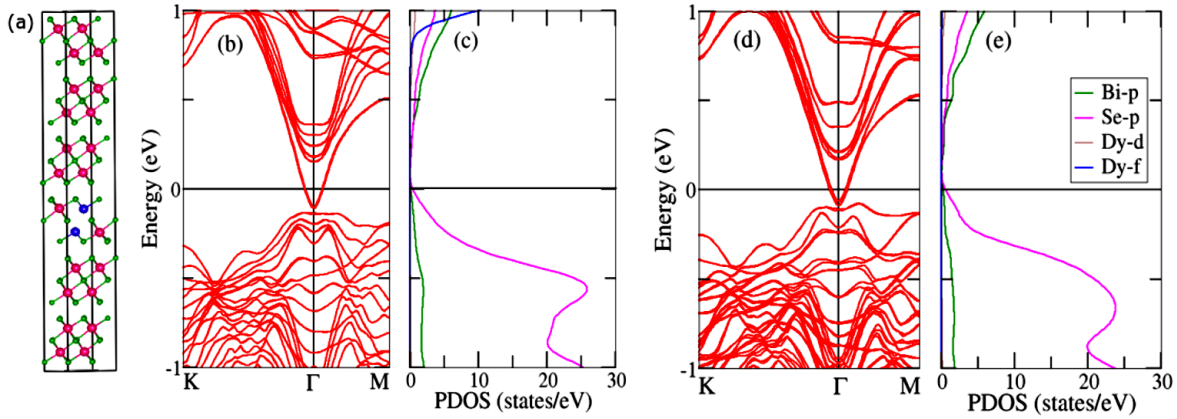

Figure 6.6: (a) Predicted lowest energy configuration for two Dy doped Bi_2Se_3. The color code followed for Bi: Magenta, Se: light green and Dy: blue. Calculated band structure along with projected density of states for bulk (b,c) and surface (d,e) states, respectively.

Further, to explore the electronic structure of Dy doped bulk Bi_2Se_3, we have adopted 2x1x2 size supercell into computations. We carried out electronic band structure and density of states (DOS) calculations including the spin-orbit coupling interaction by using GGA. The GGA functional is not able to describe electronic band structure of Dy incorporated Bi_2Se_3 besides well-known drawback i.e., severely underestimation of energy band gap. To overcome this difficulty, we switch over more appropriate exchange correlation functional i.e. GGA+U. It has been established that incorporation of Hubbard term (U) into GGA provides good description of *f*-states of element [164]. This motivate us

to incorporate GGA+U [163] calculations with U=7.0 eV as suggested in Ref. [164]. The calculated band structure has been plotted for momentum space in the direction of K-Γ-M of Brillouin zone. From figure 6.6 (b), it is obvious that there is an energy band gap at Γ ~ 25 meV. Interestingly the conduction band minimum crosses the Fermi energy level which is in agreement to measured ARPES data. In order to know the hybridization between atomic orbital, we have plotted projected density of states (PDOS), as shown in figure 6.6 (c). A sharp peak appears around -0.1 eV due to Se-*p* orbital which hybridize mainly with Bi-*p* orbital, resulting the valence band edge. However, at about 0.1 eV there is strong mixing among Bi-*p*, Se-*p*, Dy-*d* and Dy-*f* orbitals in conduction band region. It is observed that for the surface band structure of Dy-doped Bi_2Se_3 at Γ the energy band gap reduces (figure 6.6 (d)). However, there is strong mixing of Se-*p* and Dy-*d* orbital with some contribution of Bi-*p* orbitals, as has been illustrated in figure 6.6 (e).

Configuration	Dy-Dy distance (Å)	ΔE (meV)
1	4.13	-0.6
2	7.16	-0.5
3	4.26	-1.4
4	5.89	2.6
5	6.02	-0.1
6	7.30	-0.7

Table 6.1: Considered configurations for doping of Dy into Bi_2Se_3, distance (d) between two Dy atoms, and energy of magnetic ordering.

6.4 Conclusion

In conclusion, 5% Dy doped Bi_2Se_3 shows AFM order. The transition from AFM to FM occurs at very low temperature (~5 K) at ~3 T magnetic field. The appearance of surface band gap is clear and the upper value of the band gap ~ 52±4 meV at 6.5 K. Also, Dy doping in this Bi_2Se_3 TI induces Kondo effect and leads to WL to WAL crossover. The μ-SR measurements indicate that the signal measured with magnetization is reflecting the

magnetic properties of < 2(1)% of the total sample. The theoretical calculation also supports the experimental results.